Nanoscale

PAPER

View Article Online
View Journal

Cite this: DOI: 10.1039/d0nr03486j

The role of pre-nucleation clusters in the crystallization of gold nanoparticles†

Raj Kumar Ramamoorthy, *[a,b,c] Ezgi Yildirim, [a] Enguerrand Barba,[a] Pierre Roblin,[b] Jorge A. Vargas, [d,e] Lise-Marie Lacroix, [a] Isaac Rodriguez-Ruiz, [b] Philippe Decorse,[f] Valeri Petkov, [d] Sébastien Teychené *[b] and Guillaume Viau *[a]

The syntheses of metal nanoparticles by reduction in apolar solvents in the presence of long chain surfactants have proven to be extremely effective in the control of the particle size and shape. Nevertheless, the elucidation of the nucleation/growth mechanism is not straightforward because of the multiple roles played by surfactants. The nucleation stage, in particular, is very difficult to describe precisely and requires *in situ* and time-resolved techniques. Here, relying on *in situ* small angle X-ray scattering (SAXS), X-ray absorption spectroscopy (XAS) and high-energy X-ray diffraction (HE-XRD), we propose that ultra-small gold particles prepared by reduction of gold chloride in a solution of oleylamine (OY) in hexane with triisopropylsilane do not follow a classical nucleation process but result from pre-nucleation clusters (PNCs). These PNCs contain Au(III) and Au(I) precursors; they are almost stable in size during the induction stage, as shown by SAXS, prior to undergoing a very fast shrinkage during the nucleation stage. The gold speciation as a function of time deduced from the XAS spectra has been analyzed through multi-step reaction pathways comprising both highly reactive species, involved in the nucleation and growth stages, and poorly reactive species acting as a reservoir for the reactive species. The duration of the induction period is related to the reactivity of the gold precursors, which is tuned by the coordination of OY to the gold complexes, while the nucleation stage was found to depend on the size and reactivity of the PNCs. The role of the PNCs in determining the final particle size and structure is also discussed in relation to previous studies. The multiple roles of OY, as the solubilizing agent of the gold salt, the ligand of the gold complexes determining both the size of the PNCs and the reactivity of the gold precursors, and finally the capping agent of the final gold particles as oleylammonium chloride, have been clearly established. This work opens new perspectives to synthesize metal NPs *via* metal–organic PNCs and to define new synthesis routes for nanoparticles that may present structure and morphologies different from those obtained by the classical nucleation routes.

Received 4th May 2020,
Accepted 2nd July 2020

DOI: 10.1039/d0nr03486j

rsc.li/nanoscale

1. Introduction

Intense research has been carried out over the past 20 years on the growth of metallic nanoparticles (NPs) by liquid phase processes for a precise control of the particle size,[1] shape,[2] and surface chemistry[3] opening applications in biology,[4] nanoelectronics,[5] or catalysis.[6] In this field, huge progress has been made, for example, on the use of heterogeneous nucleation by seed-mediated growth methods.[7,8] Until recent times, the formation of metal NPs in solution has been described by the classical nucleation/growth theory but several studies stressed on the possibility of non-classical nucleation pathways depending on the chemical and physico-chemical conditions of the reaction.[9] Detailed knowledge of the nucleation mechanisms is of paramount importance for the control of the particle morphology.[10] However, due to its stochastic nature, observing

[a]Université de Toulouse, Laboratoire de Physique et Chimie des Nano-Objets UMR 5215 INSA, CNRS, UPS, 135 avenue de Rangueil, F-31077 Toulouse cedex 4, France. E-mail: rajrk37@gmail.com, guillaume.viau@insa-toulouse.fr
[b]Laboratoire de Génie Chimique, Université de Toulouse, CNRS, INP, UPS Toulouse, France. E-mail: sebastien.teychene@toulouse-inp.fr
[c]Fédération de Recherche FERMaT, Université de Toulouse, CNRS, INP, INSA, UPS, Toulouse, France
[d]Department of Physics, Central Michigan University, Mt. Pleasant, MI-48858, USA
[e]Unidad Académica de Física, Universidad Autónoma de Zacatecas, Calz. Solidaridad esq. Paseo de la Bufa s/n, Zacatecas, Mexico
[f]Université de Paris, ITODYS UMR 7086, 15 rue Jean-Antoine de Baïf, 75013 Paris, France

†Electronic supplementary information (ESI) available. See DOI: 10.1039/d0nr03486j

experimentally the homogeneous nucleation stage can be extremely challenging and requires *in situ* and real time techniques, such as a combination of *in situ* X-ray absorption (XAS) and small angle X-ray scattering (SAXS)[11] or *in situ* electron microscopy.[12]

In the classical nucleation theory (CNT), nucleation is the crossing of the activation energy barrier, resulting from the contribution of the volume and surface to the free energy of the nuclei. In the case of the synthesis of metal particles in solution by the reduction of a metal precursor, the CNT assumes the formation of zero-valent metal atoms and the clustering of these atoms, nucleation being the event when the clusters reach the critical size. This size is obtained when the concentration of the zero-valent atoms exceeds the supersaturation threshold. After the nucleation step, these critical size nuclei further grow. Considering an atom-by-atom growth, the final particle size is given by the nucleation rate. Experimental studies on gold nanoparticles, combining SAXS and UV-visible spectroscopy or XAS, have shown a very good agreement with the CNT.[13–15] In addition, thanks to kinetic modeling, these studies have identified the surface reaction as the limiting step of the particle growth. The formation of silver nanoparticles studied by *in situ* electron microscopy was found to follow the classical nucleation with the existence of a nucleation threshold.[12]

In the case of metal nanoparticles, an alternative model to the CNT has been proposed, in which the nucleation does not require a supersaturation threshold of zero-valent metal atoms, but occurs *via* the successive formation of dimers, trimers ... and then clusters. The nanoparticle growth is then described by an autocatalytic process at the surface of the metal clusters.[16] In that case, the separation between the nucleation and the growth stages is attained if the growth rate is much higher than the nucleation rate.[17] A slightly different pathway consists in the formation of partially reduced clusters followed by their reduction into zerovalent metal clusters.[18,19] In the case of Au NPs synthesized by reduction of gold chloride with citric acid in the presence of PVP, such a pathway *via* complex clusters has been supported experimentally by XAS showing a progressive contraction of the Au–Au distance during the nucleation stage, followed by a further increase during the growth stage.[20]

Several recent reviews described non-classical nucleation processes involved in the crystallization of bulk solids and nanoparticles.[21–25] These processes occur *via* more complex free-energy landscapes than the single nucleation barrier of the classical theory, involving stable pre-nucleation clusters (PNCs), as in the case of $CaCO_3$,[26] or metastable intermediate states with an amorphous structure, as in the case of YVO_4:Eu.[27] Few examples of non-classical nucleation have been described in the case of metal nanoparticles. An *in situ* electron microscopy study revealed the formation of gold particles from a homogeneous solution, through three clearly identified stages: an initial spinodal decomposition of the solution into metal-rich and metal-poor phases, a condensation of amorphous clusters in the metal-rich phases and a third step of crystallization of the metal particles.[28] Formation of dense liquid droplets in which the nucleation and coalescence of the first nuclei occur was observed in the classical citrate synthesis of gold nanoparticles using atomic force microscopy (AFM), dynamic light scattering (DLS) and SAXS.[29,30] Such intermediate structures are not specific to aqueous solutions. In organic solvent media, unreduced mesoscopic structures were also identified by DLS in the case of reduction of gold chloride in a solution of oleylamine in octadecene.[31]

Among the different methods, the synthesis of metal nanoparticles in apolar solvents, using long alkyl chain surfactants to control the colloidal stability of the final suspensions, is nowadays a very popular method, for both noble[32] and non-noble metals.[33] The major property sought in alkyl chain surfactants is their role in controlling the growth step, leading to a fine control of the particle size and shape.[34] However, capping agents such as long chain carboxylic acids[35] or long chain amines[36] are also ligands of the metal precursors. The stability of metal complexes, their structure, their self-organization and their solubility are all factors that can play a determining role in the reaction, the latter therefore depending on the surfactant concentration and on their association constant with the metallic ions. Disentangling the multiple roles of the surfactants at the different stages of the reaction is an important task to improve control over particle morphology and to have a better understanding of their nucleation/growth mechanism.[14,37]

Gold chloride reduction in oleylamine (OY) solution in hexane, with triisopropylsilane as the reducing agent, is a very simple method to synthesize at room temperature Au NPs with original properties. This is a unique method to synthesize monodisperse ultrathin gold nanowires with very high yield[38] that has been used by several groups with applications in different fields, such as transparent electronics.[39–41] By varying the OY concentration, it is also possible to prepare ultrasmall nanospheres by the same method and, interestingly, regardless of their shapes both kinds of particles synthesized at room temperature exhibit an atomic structure different from the fcc structure of bulk Au.[42]

In this paper, we present a detailed description of the role of OY in the nucleation/growth mechanism of Au NPs relying on *in situ* XAS, SAXS and high-energy X-ray diffraction (HE-XRD) studies performed during syntheses carried out with different OY concentrations. Only a few experimental studies were devoted to the nucleation and growth mechanism of NPs prepared by these methods, and exclusively to nanowires characterized using *in situ* techniques, SAXS,[43,44] DLS,[45] or a combination of XAS and SAXS.[46] Here, the speciation of Au in the different oxidation states was deduced from the time-resolved XAS spectra. The speciation with different OY concentrations was analyzed through multi-step reaction pathways comprising highly reactive species involved in the nucleation and growth stages and poorly reactive species acting as a reservoir for the reactive species. The reactivity of the different species and the "size" of the reservoirs have

been interpreted as dependent on the OY coordination at the Au complexes. The time-resolved SAXS study has revealed the presence of pre-nucleation clusters (PNCs) which are involved in the nucleation stage and the size of which depends on the OY concentration. A short Au–Au distance observed in the HE-XRD pattern of the PNCs has been interpreted as an aurophilic bond. The role of PNCs in determining the final particle size and structure is discussed.

2. Experimental details

2.1 Synthesis

Gold nanoparticles. Chemicals were used as received for all syntheses: hydrogen tetrachloroaurate trihydrate ($HAuCl_4{\cdot}3H_2O$, 99.99%, Alfa Aesar), triisopropylsilane (TIPS, 98%, Sigma-Aldrich), oleylamine (OY, 80–90%, Acros) and hexane (mixed isomer, 98+%, Alfa Aesar). Syntheses of Au nanospheres and nanowires were performed by reduction of $HAuCl_4{\cdot}3H_2O$ by TIPS in a solution of OY in hexane following the procedures described in ref. 42. For all syntheses, the final nominal concentration of Au and TIPS in hexane was kept constant at 20 mM and 1 M, respectively. OY concentration was varied from 50 mM to 400 mM. $HAuCl_4{\cdot}3H_2O$ was dissolved in 2 mL of solution of OY in hexane. For the lower concentration of OY, the precursor suspension was sonicated for 5 min to help the dissolution. The Au/OY solution in hexane is pale yellow and orange color for the lowest and the highest concentrations of OY, respectively. Then, 512 μL of TIPS was added into the Au/OY solutions. By mixing the TIPS, the solution containing 50 mM OY turns from pale yellow to dark brown-red within few seconds while the solutions containing 100 mM and 400 mM OY take around 10 min and a few hours, respectively, to reach the same color. The particles prepared with [OY] = 50 and 100 mM were analyzed after 3 h of reaction, and the particles prepared with [OY] = 400 mM were analyzed after 24 h of reaction.

TIPS can be formally considered as a hydride. The stoichiometry of the chemical reduction of $HAuCl_4$ by TIPS in the presence of OY can be written as:

$$HAuCl_4 + \frac{3}{2}R_3SiH + \frac{5}{2}C_{18}H_{35}NH_2 \rightarrow Au(0) + \frac{3}{2}R_3SiCl + \frac{5}{2}C_{18}H_{35}NH_3{}^+Cl^- \quad (1)$$

Thus, TIPS was always introduced in very large excess with respect to the stoichiometry. The experimental conditions with [OY] = 50 mM correspond to the stoichiometry while with [OY] = 100 mM and 400 mM OY was introduced in excess.

***In situ* experiments.** For the *in situ* SAXS and XAS experiments (see below), 3 mL of a solution containing $HAuCl_4{\cdot}3H_2O$ (40 mM) and OY (100 mM, 200 mM or 800 mM) dissolved in hexane and 3 mL of a TIPS (2 M) solution in hexane were prepared. The chemical reduction was achieved by injecting an equal volume of $HAuCl_4$/OY solution and TIPS solution, at a rate of 10 ml min^{-1}, in a T-micromixer (IDEX-HS P-712) using PHD 22/2000 syringe pumps (Harvard apparatus). The mixing time, estimated from the Falk and Commenge correlation, is 40 ms.[47] The reactions were carried out in a glass capillary and in a PMMA cuvette for SAXS and XAS analysis, respectively (see Scheme S1 in the ESI†).

Au(I) intermediate compound. $HAuCl_4{\cdot}3H_2O$ (20 mM) was dissolved in pure OY (5 mL) and left at room temperature for 48 h. A white precipitate that appeared is a lamellar phase as already described in ref. 44. In the present study, this compound has been used as a Au(I) reference for XAS analysis. The *in situ* X-ray absorption spectrum at the Au L_{III}-edge of this compound was correctly fitted with approximately two N at a distance of 2.09 Å (Table 1). More details about the XAS spectrum and Extended X-ray Absorption Fine Structure (EXAFS) fit are given in the ESI (Fig. S7†). The presence of only two light atoms in the Au coordination sphere and the atomic ratio Au/Cl = 1 measured by XPS confirmed that Au has the oxidation state +1 in this compound.

Table 1 Coordination number, *N*, bond length, *R*, and Debye–Waller factor, σ^2, of the first coordination shell around Au fitted to EXAFS spectra of Au(III) precursors, Au(I) intermediate phase, Au(0) nanospheres and nanowires and gold foil. Figures in brackets indicate the uncertainties of the last digit as estimated after fitting FT EXAFS over three different *q*-ranges

	N_{Au-Cl}	R_{Au-Cl} (Å)	σ^2_{Au-Cl} (Å^2)	N_{Au-N}	R_{Au-N} (Å)	σ^2_{Au-N} (Å^2)
Au(III) precursors						
[OY] = 50 mM	4.1(2)	2.23(1)	0.005(1)	—	—	—
[OY] = 100 mM	1.5(1)	2.28(1)	0.005(1)	2.5(1)	2.02(1)	0.005(1)
[OY] = 400 mM	—	—	—	4.1(6)	2.06(1)	0.006(2)
Au(I) intermediate						
Au(I)-OY	—	—	—	2.1(1)	2.09(1)	0.004(1)
	N_{Au-Cl}	R_{Au-Cl} (Å)	σ^2_{Au-Cl} (Å^2)	N_{Au-Au}	R_{Au-Au} (Å)	σ^2_{Au-Au} (Å^2)
Au(0) nanoparticles						
NSs [OY] = 50 mM	0.7(1)	2.41(1)	0.004(1)	8.5(5)	2.84(1)	0.014(1)
NWs [OY] = 400 mM	0.8(1)	2.37(1)	0.009(1)	9.0(4)	2.86(1)	0.011(1)
Au foil reference	—	—	—	12	2.88(1)	0.008(1)

2.2 *Ex situ* characterization

Ex situ transmission electron microscopy (TEM) images were captured using a JEOL-JEM 1400 instrument at an operating voltage of 120 kV. The colloidal suspensions were diluted in hexane and one drop was deposited on a TEM grid covered with a thin carbon film. *Ex situ* X-ray photoelectron spectroscopy (XPS) spectra were recorded using a K-Alpha$^+$ system (ThermoFisher Scientific, East-Grinsted, UK) fitted with a micro-focused and monochromatic Al Kα X-ray source (1486.6 eV, spot size of 400 μm). The spectrometer pass energy was set to 150 and 40 eV for the survey and the narrow high resolution regions, respectively. Several drops of the colloidal suspension prepared with the lowest OY concentration were deposited on a silicon substrate. For the nanoparticles prepared with [OY] = 100 and 400 mM, the excess of OY was removed from the suspensions. The colloidal suspensions (1 mL) were mixed with absolute ethanol (3 mL) and centrifuged at 4000 rpm for 5 min. The supernatant was discarded and the particles were re-dispersed in pure hexane. Several drops of the purified suspensions were deposited on a Si substrate. *Ex situ* X-ray diffraction (XRD) at wide angles was carried out on a Panalytical Empyrean diffractometer equipped with a Co Kα X-ray source, a Bragg–Brentano HD primary optics and a linear Pixcel1D detector. The nanoparticles were centrifuged at 4000 rpm for 5 min after addition of an OY solution in absolute ethanol (3 mL) to the mother liquor (1 mL). The supernatant was discarded and the particles were redispersed in a small volume of hexane. Several drops of the particle suspensions were deposited on a zero-background silicon substrate and dried in air. The patterns were recorded with a step size of 0.8° and a time per step of 250 s.

2.3 *In situ* studies

SAXS, XAS and HE-XRD measurements were performed in a static mode, during and after the completion of a reaction. For the kinetic studies, the glass capillaries and PMMA cuvettes were filled using the mixing procedure described in section 2.1 for the synthesis of gold nanoparticles. In the case of 2.5 mL PMMA cuvettes for XAS experiments, the dead volume was 0.75 mL (Scheme S1 in the ESI†). With a total flow rate of 20 mL min^{-1}, the dead volume was filled after 2.25 s. The first XAS acquisition time after mixing was 4 s. For SAXS experiments, the very small dead volume in the capillaries allowed capturing the SAXS signal at the very beginning of the reaction.

In situ SAXS synchrotron experiments were carried out at the SWING beamline (SOLEIL, France) and at the c-SAXS beamline (PSI, Switzerland). SAXS measurements were performed in the transmission mode with an X-ray source energy of 12.5 keV and 11.5 keV. A glass capillary with a diameter of 1.5 mm was used for each measurement. *In situ* SAXS signals were acquired every 2 s for the syntheses with [OY] = 50 and 100 mM, and every 1 min 10 s for the syntheses with [OY] = 400 mM. At PSI, time-resolved SAXS signals were recorded at a distance of 2.17 m using a PILATUS 2 M. At SWING, time-resolved SAXS signals were recorded at two distances of 6.07 m and 0.5 m using an Eiger X 4 M (Dectris). Each reaction was performed twice with the SAXS detector at the two different distances. For further analysis, the SAXS signals recorded at the two distances were merged in the region q = 0.15–0.2 Å^{-1}. The nice overlap of the SAXS signals recorded from the two detector positions, all along the reaction time, indicated the reproducibility of the reactions. SAXS patterns, before and after the nanoparticle nucleation, were analyzed with a Beaucage model,[48] using a homemade python script. The detailed description of the fitting model and the procedure are presented in the ESI.†

In situ energy dispersive XAS experiments were carried out at the ODE beamline (SOLEIL, France). The XAS was recorded at the Au L_{III}-edge in transmission mode. Due to the low concentration of Au, a PMMA cuvette of 10 mm was employed for XAS studies. Time-resolved XAS signals were recorded every 0.36 s for the syntheses with [OY] = 50 and 100 mM and 3.8 s for the syntheses with [OY] = 400 mM. Athena[49] and Larch[50] software modules were used for extraction and best-fitting of the EXAFS spectra, respectively. The software PrestoPronto[51] was used for the linear combination analysis (LCA) of the XAS spectra. EXAFS spectra were Fourier transformed (FT), over three different q ranges, 2 Å^{-1}–8.5 Å^{-1}, 2.5 Å^{-1}–8.5 Å^{-1} and 2 Å^{-1}–9.0 Å^{-1}, using the Hanning window and fitted in "*R*" space to extract the first and second shell EXAFS parameters, along with the uncertainty values, around the Au absorber. The amplitude and phase shift functions of Au–Cl and Au–N bonds and of Au–Au were calculated from the structure of the aminochloroaurate(III), $AuCl_3NH_3$ (crystallographic open database file no. 1532148),[52] and from bulk fcc Au, respectively, using FEFF8.4.[53] The time-resolved XAS spectrum of each synthesis was analyzed by LCA with three spectra: precursor solution, intermediate compound and final gold particles. This method provided an assessment of the gold speciation as a function of time. More details are given in the ESI.†

In situ HE-XRD experiments were carried out at the 11-ID-B beamline (Advanced Photon Source, Argonne). Samples were contained in thin-walled glass capillaries. The particles were analyzed in suspension in the mother liquor. X-rays with an energy of 58.62 keV (λ = 0.2115 Å) were used, and the scattered intensities were collected with a large area (amorphous Si) detector. The patterns covered wave vectors in the range of 1 Å^{-1} to 25 Å^{-1} with a q-space resolution proven acceptable for atomic pair distribution function (PDF) studies. The acquisition time was 1 min for each spectrum, ruling out the possibility of monitoring the reaction in real time for [OY] = 50 mM. HE-XRD data for an empty capillary and pure solvents were taken separately and used to correct the HE-XRD patterns for the Au suspensions. Several structure models were tested to describe the experimental PDFs. The models were relaxed in terms of energy and then equilibrated at room temperature by classical molecular dynamics (MD). Best MD models for Au NPs and NWs were refined against the experimental data with a reverse Monte Carlo technique.

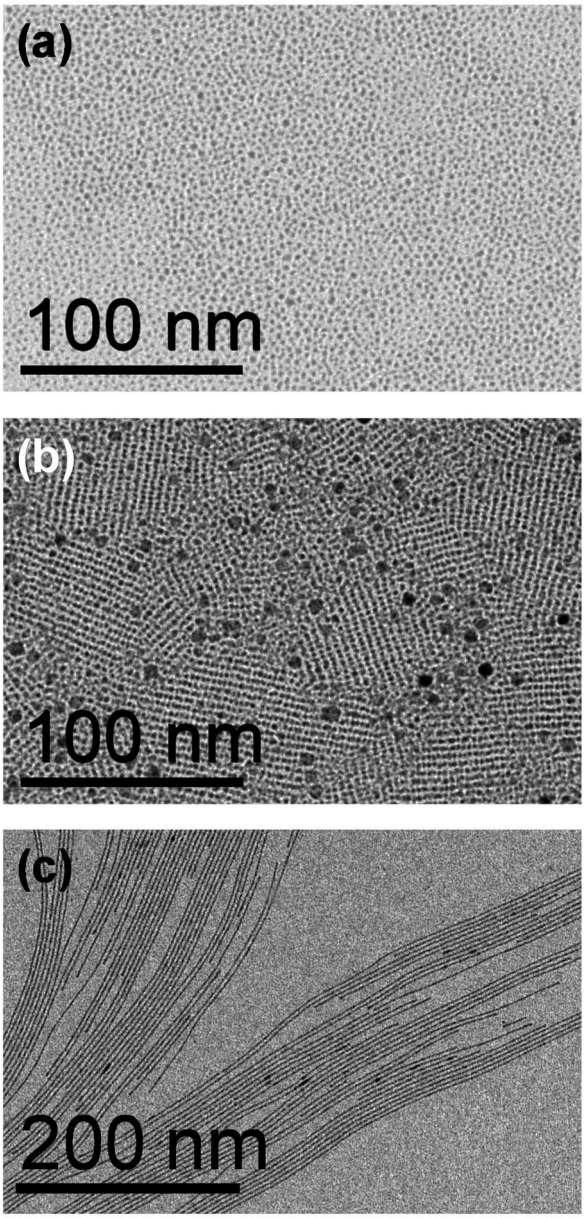

Fig. 1 Transmission electron microscopy images of nanoparticles and nanowires prepared with different concentrations of oleylamine: (a) [OY] = 50 mM, isotropic particles with a mean diameter d_m = 2.2 nm (σ/d_m = 13%); (b) [OY] = 100 mM, isotropic particles with bimodal size distribution d_m = 2.2 nm (σ/d_m = 11%) and 5.9 nm (σ/d_m = 21%);(c) [OY] = 400 mM, nanowires with a mean diameter d_m = 2.0 nm (σ/d_m = 13%). Particles were deposited on TEM grids after 3 h of reaction (a) and (b), or after 24 h (c).

3. Results and discussion

3.1 Au nanoparticle morphology and structure

Fig. 1 shows representative TEM images of the final Au nanoparticles, prepared by reduction of $HAuCl_4{\cdot}3H_2O$ in solution of OY in hexane, with a large excess of TIPS, for three different OY concentrations. For [OY] = 50 mM, isotropic particles with a mean diameter of 2.2 nm are observed. After 30 min of reaction, the final particle size does not vary with time. The nanoparticles observed after 3 h and 24 h exhibit the same mean diameter and same standard deviation of the size distribution (see ESI, Fig. S1†). The nanoparticle morphology is very dependent on the OY concentration. A bimodal distribution of isotropic particles, a major population with a mean diameter of 2.2 and a minor population of 5.9 nm were found for [OY] = 100 mM after 3 h of reaction. The smallest particles self-organized on the TEM grid, while the largest ones are located at the grain boundaries of the small particle super-lattices (Fig. 1b). For [OY] = 400 mM, the reaction is much slower and the particle growth is completely different with the formation of nanowires (NWs) exhibiting a mean diameter of 2.0 nm and length of several micrometers. With the average diameter of the spheres and wires prepared with [OY] = 50 and 400 mM, respectively, being almost the same, the ratio between the volumes of the two types of particles is greater than several thousand. Therefore, oleylamine does not only act as a simple capping agent of the final particles but also plays a crucial role in the nucleation rate.

The XRD patterns of the different samples exhibited very broad bands in agreement with the very small diameter of the particles (ESI, Fig. S2†). The comparison with the expected positions of the different reflections for the fcc structure of Au suggests a structure different from the bulk. It is noteworthy that the structure of the synthesized NPs is very different from the one of those prepared with ammonium borohydride or amino borane as the reductant that crystallize with the classical fcc structure.[13,15] Structural models required HEXRD and pair distribution function (PDF) analysis. The experimental PDFs are given in Fig. 2 along with the best fits obtained from the 3D models shown as insets. In order to make a fair comparison, the PDF of a truncated octahedron nanoparticle with

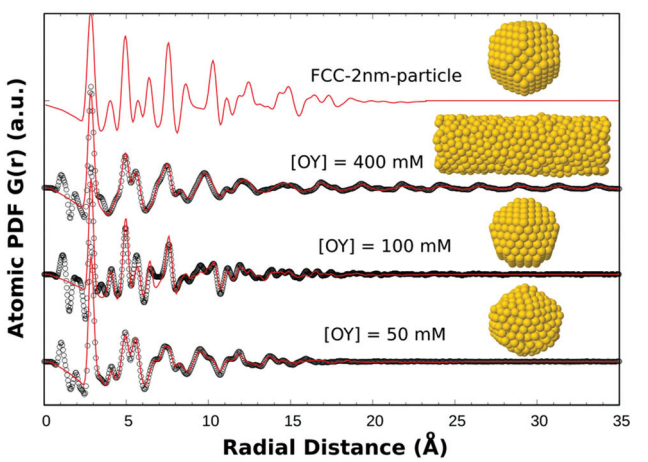

Fig. 2 *In situ* atomic pair distribution function of Au nanoparticles prepared by reduction of $HAuCl_4{\cdot}3H_2O$ in OY solution in hexane at different OY concentrations (black circles) and best PDF fits (red lines) obtained from the atomic models presented as insets: distorted icosahedron for [OY] = 50 mM, Marks decahedron for [OY] = 100 mM and wire with a tcp structure derived from the α-Mn crystal structure. The theoretical PDF of a truncated octahedron with a fcc crystal structure is also given for comparison.

a fcc structure is presented in the same figure. It is clear that none of the Au nanoparticles synthesized here exhibits a fcc structure. The agreement between the experimental and simulated PDFs is remarkable allowing us to talk about the atomic ordering with confidence. The nanoparticles obtained with [OY] = 50 and 100 mM are well described by distorted icosahedra and Marks decahedra, respectively, while the nanowires obtained with [OY] = 400 mM exhibit a distinctive lack of the fcc second neighbor distance about r = 4 Å, also present in icosahedral and decahedral structures. This led us to propose a tetrahedrally close packed structure derived from the α-Mn structure incorporating distorted icosahedra and larger size coordination polyhedra, as reported in our previous work.[42] According to the first feature of the PDFs, the first-neighbor Au–Au pair distance is found at about 2.86 Å, which is slightly smaller than the Au–Au bonding distance in bulk Au (2.88 Å).

The XAS at the Au L_{III}-edge of nanospheres and nanowires are given in Fig. S3 of the ESI† with the fits to the EXAFS spectra. The coordination number (N), the bond distance (R) and the Debye–Waller factor (σ^2) deduced from these fits are given in Table 1. Two distinct atom shells were needed to fit the EXAFS spectra. Around the Au absorber, 0.7 Cl and 8.5 Au atoms, and 0.8 Cl and 9 Au atoms are found for the nanospheres and the nanowires, respectively (Table 1). Under the same conditions, the N_{Au-Au} coordination number was found to be equal to 12 in the Au foil, as expected for the bulk metal with a fcc structure. The lower N_{Au-Au} coordination number determined here in both cases is related to the small particle diameter. For 2.2 nm gold NPs, 50% of the Au atoms are located at the surface and therefore are uncoordinated. For the nanowires, the relative amount of undercoordinated surface atoms was estimated as 43%.[42] The Au–Au distances of 2.84 Å and 2.86 Å found in the nanospheres and nanowires, respectively, are in good agreement with the PDF results and previous XAS studies on ultrasmall gold particles.[20,54]

The XPS survey scans of the particles prepared with [OY] = 50 mM exhibited Au 4f, C 1s, N 1s, and Cl 2p peaks centered at *ca.* 84, 285, 400, and 198 eV, respectively (ESI, Fig. S4†). The Au $4f_{7/2}$ and $4f_{5/2}$ high-resolution spectra were fitted with a single component corresponding to Au(0). The N 1s high-resolution spectrum revealed a main peak centered at 401.3 eV corresponding to the binding energy of oleylammonium cation N atoms.[55] The molar ratio ammonium/chlorine calculated from the integrated intensity of the two respective peaks was found to be equal to 1 in agreement with the formation of the oleylammonium chloride. A minor peak, centered at 399.2 eV, corresponds to the binding energy of oleylamine N atoms. The relative intensity of OY represented only 7% of the total N 1s intensity showing that for the molar ratio Au/OY = 2.5, the conversion of OY into ammonium is almost complete in agreement with the stoichiometry of eqn (1). For the nanospheres and nanowires prepared with an excess of OY, the N 1s high-resolution spectrum exhibited two contributions centered at the same energy of 401.3 and 399.5 eV.[43] Under such conditions, only a part of OY was converted to ammonium which was nevertheless clearly identified in the XPS spectrum, despite the washing. We can thus conclude that the oleylammonium chloride is strongly bound to the gold NP surface, in agreement with adsorption energy calculations.[56]

3.2 Influence of [OY] on the Au(III) precursor/*in situ* study of the Au(III) precursors

The precursor solutions, prepared by dissolution of $HAuCl_4{\cdot}3H_2O$ in hexane with different OY concentrations, were studied both by XAS and by SAXS prior to the addition of TIPS.

The XAS spectra of the precursor solutions exhibit an intense white line peak "A" at 11 921.2 eV, characteristic of the Au complex in the +3 oxidation state (ESI, Fig. S5a†). An increasing intensity of the feature "C" at 11 934 eV and a slight shift of the white line towards high energy are observed with increasing OY concentration (Fig. S5a,† inset). To evaluate the local changes of the Au coordination sphere in the different precursors, the FT of the EXAFS signals was fitted in R-space using the amplitude and phase shift functions of reference files calculated by FEFF8.4 (see Experimental details). The fitted curves of the different Au precursors are presented in the ESI (Fig. S5b–d†) and the fit parameters to the first coordination shell are summarized in Table 1. For [OY] = 50 mM, 4 Cl atoms at the distance R = 2.23 Å are found in the first coordination shell of Au. These values are consistent with the formation of $[AuCl_4]^-$ OY^+ ion pairs when $HAuCl_4$ is dissolved in the solution of OY in hexane. As a matter of comparison, the Au–Cl bond length is between 2.23 and 2.34 Å in the dimer Au_2Cl_3 in the solid state,[57] and takes an average value of 2.277 and 2.274 Å in $NaAuCl_4$ and NR_4AuCl_4, respectively.[58,59] With increasing [OY], the chlorine atoms of the coordination shell are progressively replaced by nitrogen. A mixed Cl/N coordination shell is found for [OY] = 100 mM and four N atoms as first neighbors are found for [OY] = 400 mM. The bond length R_{Au-N} is found between 2.02 and 2.06 Å (Table 1). The Au–N bond length is a little bit longer than that in $AuCl_3NH_3$,[52] but similar to the bond length measured by EXAFS in a solution of $HAuCl_4$ in hexane with an excess of OY.[46] This complexation of the Au(III) ions by OY is also revealed by a change in the color of the solution, from pale yellow with [OY] = 50 mM to dark orange with [OY] = 400 mM.

The SAXS patterns of the different precursor solutions are shown in Fig. 3. Whatever the OY concentration, the scattering intensity exhibits a Guinier regime in the intermediate-q region and a Porod regime in the high-q region. Since the organic molecules, OY and TIPS, exhibit almost the same scattering length density (SLD) as hexane (Table S1†) they cannot be responsible for the scattering intensity at small angles. In contrast, the SLD of the ion pair $[AuCl_4]^-OY^+$ and the one of gold chloride coordinated with OY are estimated as almost twice the SLD of hexane (Table S1†). Thus, the observed scattering intensity is interpreted as the presence of molecular clusters of Au(III) complexes in solution. These clusters will be further referred to as pre-nucleation clusters (PNCs). Note that in the case of [OY] = 100 mM, the increasing intensity at very small q can reveal the presence of secondary structures resulting from the assembly of PNCs (Fig. 3). Two variations in the SAXS profiles are observed when [OY] is increased. The "knee-feature" is shifted toward

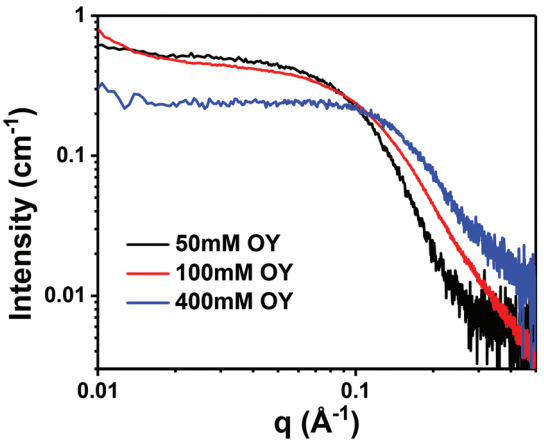

Fig. 3 SAXS pattern of the initial precursors obtained by dissolving $HAuCl_4$ in a solution of OY in hexane at the OY concentrations of 50 mM (black line), 100 mM (red line) and 400 mM (blue line).

high-q, from about 0.08 $Å^{-1}$ for [OY] = 50 mM to 0.12 $Å^{-1}$ for [OY] = 400 mM, and the slope of the Porod regime is decreasing. The radius of gyration, R_g, and the exponent of the power law in the Porod regime, p, were determined by fitting a Beaucage equation to the SAXS profiles (see ESI, Fig. S6†). Assuming spherical objects, the average diameter was calculated from the relationship $D_{SAXS} = 2\sqrt{5/3}R_g$. D_{SAXS} was found to decrease from 4.4 nm for [OY] = 50 mM, to 3.9 nm for [OY] = 100 mM and to 2.7 nm for [OY] = 400 mM (Table S2 in ESI†). The value for the higher [OY] is similar to the one previously reported by Pschunder *et al.*[46] The exponent p for the Porod law decreases from 3.5 to 2.8 for [OY] = 50 mM and 400 mM, respectively (Table S2†). These values reveal surface fractal objects, with an open shape and a rough surface. This confirms the "molecular nature" of the clusters, presumably coordination polymer chains in folded conformation. The decreasing p value indicates that the clusters transform from surface fractal to mass fractal at high [OY]. In other words, a large excess of OY limits the clustering and creates less dense zones inside more open clusters. This effect may be related to the increasing number of OY molecules coordinated to the Au atoms that can limit the clustering of the gold complexes.

3.3 *In situ* study of nucleation and growth of Au nanospheres

The nucleation and growth of the nanospheres prepared with [OY] = 50 mM were studied by *in situ* XAS and SAXS to follow both the Au speciation and the particle morphology as a function of time.

Gold speciation. Time-resolved XAS spectra recorded during the synthesis of gold nanoparticles with [OY] = 50 mM are shown in Fig. 4a. Once the addition of TIPS is performed, the EXAFS oscillations are modified, the intensity of the white line at 11 921.2 eV decreases and the intensity of the peak "B" at 11 948.5 eV increases. After 30 min, the XAS spectrum is similar to that of a Au foil, indicating that most of the Au(III) ions have been reduced to Au(0) in agreement with the XPS results. To assess the gold speciation as a function of time, time-resolved XAS spectra were fitted by the linear combination analyses (LCA), as described in previous studies.[14,31] At first, the LCA were performed with only two contributions, the spectrum of the Au(III) initial precursor at t = 0 s (Fig. S5a†) and the one of the final Au(0) nanoparticles after 24 h of reaction (Fig. S3a†). Nevertheless, the best fits of the XAS spectra left out a significant residual contribution. Based on previous growth mechanism studies[44,60,61] showing that a Au(I) phase with a layered structure could be an intermediate in the reduction of gold tetrachloride in the presence of oleylamine, the XAS spectrum of such an Au(I) phase (Fig. S7 in the ESI†), prepared with a large excess of oleylamine (see the Experimental section), was introduced as a third possible contribution in the LCA. An example of LCA is given in Fig. 4b showing the goodness of the fit. For each XAS spectrum, the relative weights of the three different components were deduced from the LCA and were attributed to the gold concentration in the three different oxidation states. The relative concentrations of Au(III), Au(I) and Au(0) are plotted for a short time range (up to 120 s) and for a longer time range (up to 25 min) in Fig. 4c and d, respectively. Three stages can be defined: the induction period, the nucleation, and the growth stage. Straight after the addition of TIPS, Au(I) is observed in the medium. The first stage, until 10 s, is referred as the induction period, during which the reduction from Au(III) to Au(I) is noticed. The second stage corresponding to the onset of Au(0) and then to the steep increase of Au(0) concentration, grey shaded area in Fig. 4c, is interpreted as the nucleation stage. During this period, the Au(I) concentration reaches the maximum value of *ca.* 35%. After t = 30 s, the increase of [Au(0)] is slowed down which is interpreted as the end of the nucleation and the beginning of the growth stage. 50% of the gold precursor has reacted during the first 30 s and the remaining 50% is reduced very progressively during the following several tens of minutes. In order to describe more precisely the nucleation/growth stages and to assess the reaction rates, an autocatalytic model was defined following Finke's approach.[16] However, a model taking into account only the two-step reduction, Au(III) → Au(I) → Au(0), and the auto-catalytic step, Au(I) + Au(0) → Au(0), was not able to describe both the very rapid variations of [Au(III)] and [Au(0)] during the nucleation stage and the very slow ones during the growth stage. The study on the Au(III) complexes with different OY concentrations showed that OY can coordinate the Au ions. In the reaction with the molar ratio [OY]/[Au] = 2.5, one equivalent of OY is used to dissolve $HAuCl_4$ in hexane through the formation of the ion pair $OY^+[AuCl_4]^-$. The 1.5 equivalents of OY remaining in solution can complex the Au ions and modify their reactivity. Competition between reduction and complexation was therefore introduced leading to a possible co-existence of reactive Au(III) and Au(I) species (schematically Au coordinated mostly with Cl) and inert species toward the reduction (schematically complexes with OY in the Au coordination sphere). In this model, the nucleation and the auto-catalytic step involve only the "reactive" Au(I) species (Scheme 1). The kinetic model is

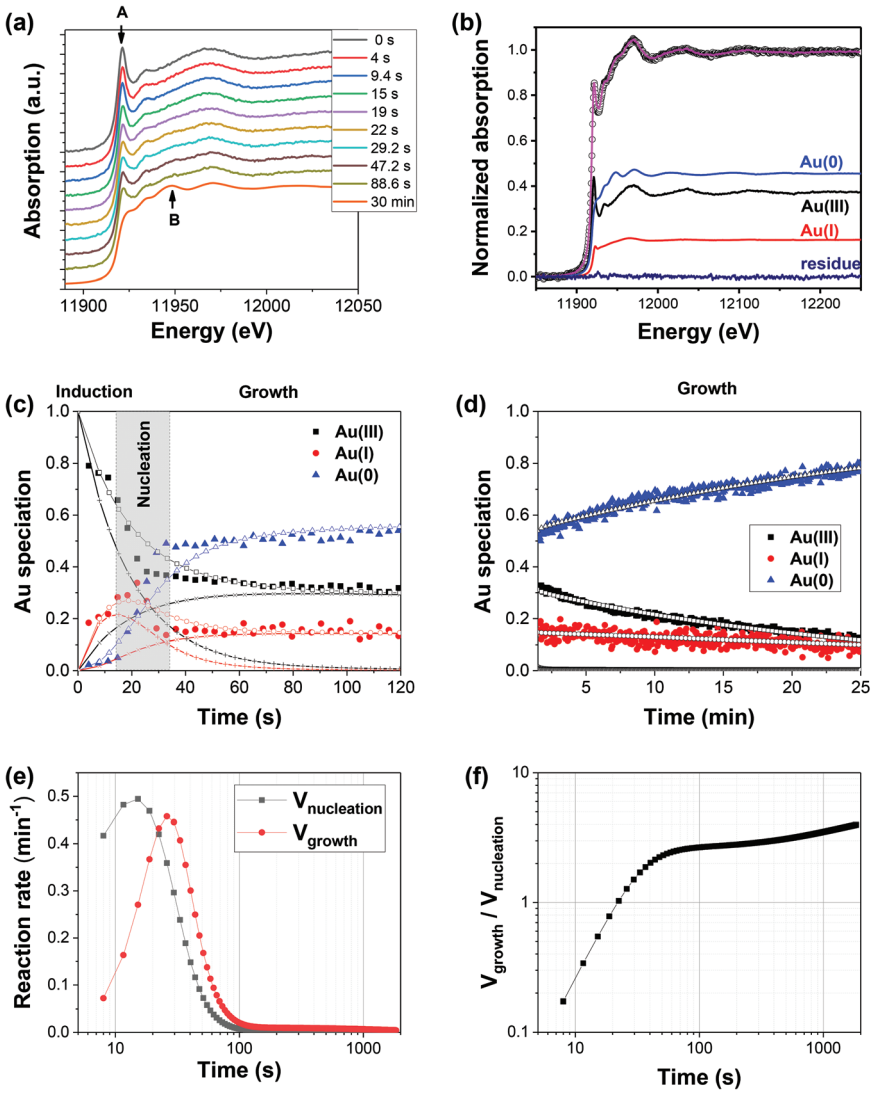

Fig. 4 (a) *In situ* XAS spectra at the Au L_{III}-edge recorded during the synthesis of Au nanoparticles in a solution of OY/hexane with [OY] = 50 mM; (b) fit of the XAS spectrum at 29 s (open circles) by a linear combination of three components (magenta line), Au(III) precursor (black line), Au(I) intermediate (red line) and final Au(0) NPs (blue line). Relative Au(III), Au(I) and Au(0) concentrations deduced from the LCA: (c) plotted between 0 and 120 s and (d) between 1.5 and 25 min. The open dots correspond to the best fit to the Au speciation, the symbols (+) correspond to the reactive Au(III) and Au(I) species, and the symbols (×) correspond to the less reactive Au(III) and Au(I) species (see text). (e) Nucleation and growth rates as a function of time given by the fit according to reaction Scheme 1; (f) ratio between the growth and nucleation rates.

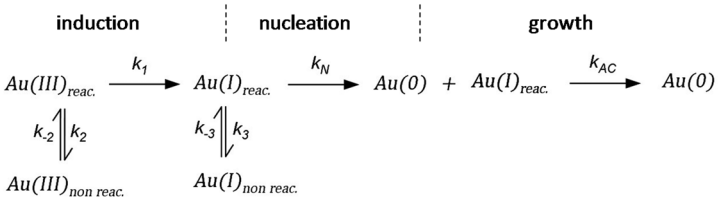

Scheme 1 Modelling of the reaction mechanism of the Au nanosphere formation with [OY] = 50 mM. The reduction pathway involves a two-step reaction, Au(III) to Au(I) and Au(I) to Au(0). The Au(0) NP nucleation/growth process is modelled by an auto-catalytic process with the reaction rate constants k_N and k_{AC}. A competition between reduction and complexation of the Au(III) and Au(I) by OY is described by two additional equilibrium during the induction stage. The two "non reactive" complexes are not directly involved in the reduction steps but serve as a reservoir for the "reactive complexes".

described with more details in the ESI (Table S3† and corresponding text). As can be seen in Fig. 4(c and d), this kinetic model describes satisfactorily the variation of [Au(III)], [Au(I)] and [Au(0)] over the entire reaction. The reactive Au(III) species are consumed very rapidly during the induction and nucleation stages, while the concentration of the reactive Au(I) species reaches a maximum value just after the onset of Au(0). During the growth stage, the concentrations of the reactive species are almost zero, both the "non-reactive" Au(III) and Au(I) species act as reservoirs, and their transformation into reactive species is the limiting step of the reaction. Thanks to the modelling of the kinetics, it is possible to plot the nucleation and growth rates as a function of time (Fig. 4e). The rate constants fitted to the gold speciation show an overlap between nucleation and growth during the steep increase of Au(0) and after 35 s the growth rate is higher than 1.9 times the nucleation rate (Fig. 4f). This time is in very good agreement with the extent of the nucleation stage deduced from the experimental curves. It is noteworthy that, experimentally, the beginning of nucleation has been taken at the onset of Au(0), *i.e.* when particles exhibiting a metallic rather than a molecular character appear in the medium because the reference for the Au(0) species in the LCA analysis was gold nanoparticles. It means that the presence of soluble Au(0) species was neglected in our analysis. This stresses the limit of the comparison between the gold speciation and the Finke's model where the nucleation is described by a single step reaction. It may explain the small discrepancy between the experimental data and the modelling at the beginning of the nucleation. The modelling was nevertheless very useful to show the presence of non-reactive species and to identify the end of the nucleation stage when V_N becomes much lower than V_{AC}.

Evolution of size – SAXS. Fig. 5 shows the time evolution of the SAXS patterns recorded during the synthesis of nanoparticles with [OY] = 50 mM, for the first 40 s of reaction, *i.e.* covering the induction and nucleation stages and the beginning of the growth stage (Fig. 5a), and between 48 s and 30 min, *i.e.* during the growth stage (Fig. 5b).

The absolute scattering intensity is almost constant between t = 4 s and 22 s *i.e.* during the induction stage. The SAXS profile is as follows: a Porod regime in the very low-q range, a Guinier regime in the intermediate-q range with a "knee-feature" and a Porod regime in the high-q range (Fig. 5a). This SAXS profile is interpreted from the presence of primary scattering objects responsible for the intensity in high- and intermediate-q ranges, these first level structures being assembled at a larger scale into secondary structures, responsible for the low-q power law. The structure of the primary objects is similar to the PNCs observed prior to the addition of TIPS (Fig. S9a†). The scattering intensity profiles were analyzed using a Beaucage equation[48] for a two level structure in order to take into account the secondary structures (see more details in the ESI, Fig. S9†). The main fitted parameters to the SAXS curves are given in Table S4.† The radius of gyration is comprised between 17 and 14.8 Å, giving a diameter D_{SAXS} that decreased from 4.4 to 3.8 nm, assuming an isotropic shape for the PNCs. The exponent of the power law at high-q is also almost constant with an average value of 3.3 (Table S4†). Thus during the induction stage, a slight shrinkage of the PNC size and almost no change in their internal

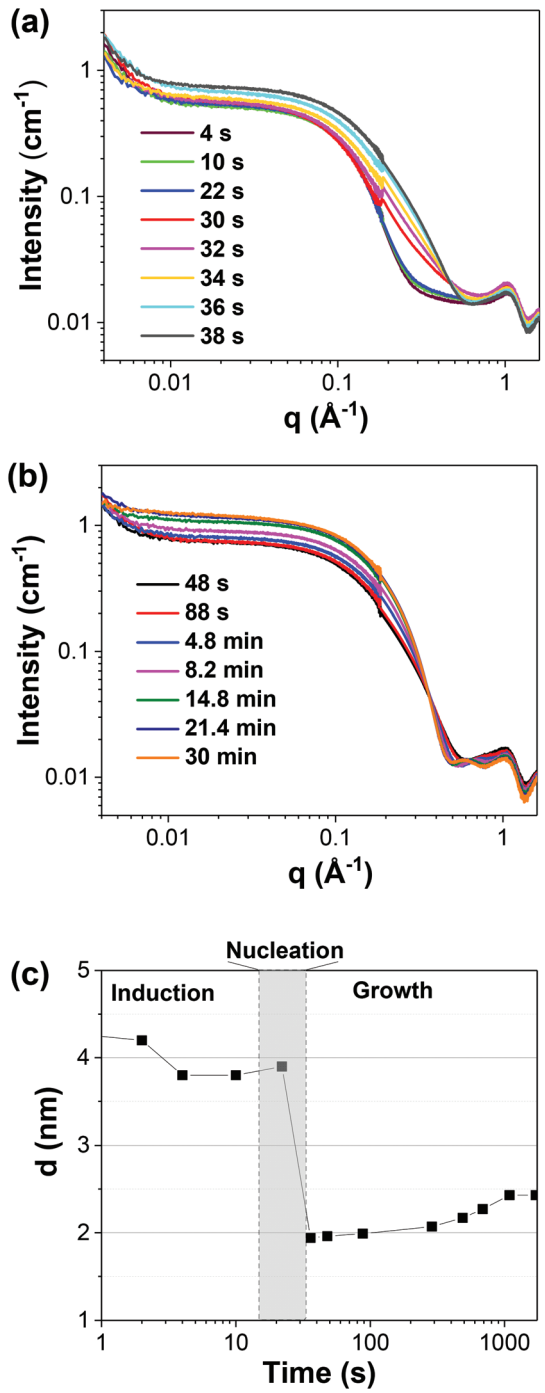

Fig. 5 *In situ* SAXS patterns recorded during the synthesis of Au nanoparticles in OY/hexane solution with [OY] = 50 mM: (a) between 4 and 40 s and (b) between 48 s and 30 min; (c) particle mean diameter as a function of time, calculated from the radius of gyration of the Au(III)–Au(I) pre-nucleation clusters during the induction stage and from that of Au(0) NPs during the growth stage. The grey shaded area corresponding to the nucleation stage was deduced from the XAS results.

structure are noticed while the XAS study showed a progressive reduction of Au(III) to Au(I) during the same period. Between 22 s and 34 s, *i.e.* during the period identified as the nucleation stage in XAS, an abrupt change of the scattering intensity profile is observed, with a very fast shift of the "knee-position" to the high-q region. Thus, for the time range corresponding to the highest [Au(0)] slope in the LCA-XAS data, a shrinkage of the particle size occurs that can be interpreted as the fast transformation of the PNCs into metal nuclei. For the period going from 48 s to 30 min, identified as the growth stage, the knee-position is progressively shifting towards low-q and the SAXS intensity in the intermediate-q range is progressively increasing, which is interpreted as a slight increase of the metal nanoparticle size. The scattering intensity profiles during the growth stage were fitted to a sum of two single level Beaucage equations corresponding to a mixture of remaining PNCs and metal NPs (see the ESI for more details, Fig. S9†). The weight of the PNCs scattering intensity, the radius of gyration and the slope of the Porod law corresponding to the SAXS intensity of the metal nanoparticles are reported in the ESI (Table S4†). When time increases, the weight of the PNCs decreases and the metal particle size increases from 1.9 to 2.4 nm (Fig. 5c). These values are consistent with the mean size measured from the TEM images. The metal NP size increase, observed during the growth stage, corresponds approximately to 1 atomic layer around the metal particles. Considering that, at these very small sizes, the addition of a 1 atom shell means an increase of 50% in the number of atoms in the particles, the size increase is consistent with the XAS analysis showing that 50% of Au was involved in the growth stage (Fig. 4). The value of the exponent of the high-q Porod regime was fixed to 3.7, equal to that of the 30 min signal. This value is close to 4, the expected value for metal particles with a smooth surface in suspension in liquid. The slight difference can be attributed to NP surface disorder and/or adsorption of unreduced species at the metal NP surface since the reduction was not complete at 30 min.

Fig. 5c summarizes the overall process including the XAS and SAXS results: – molecular pre-nucleation clusters with an almost stable size during the induction stage; – fast shrinkage of the PNCs in the time interval corresponding to the nucleation stage according to the XAS results; – slow increase of the metal NP mean size during the growth stage. The shrinkage is interpreted as the transition from molecular clusters with a long internal Au–Au distance to dense metal NPs with a shorter internal Au–Au distance.

3.4 Influence of [OY] on kinetics of nucleation and growth

Fig. 6(a and b) depict the speciation of gold species in the different oxidation states, Au(III), Au(I) and Au(0), for the syntheses with [OY] = 100 mM and 400 mM, calculated from the LCA analysis of the time-resolved XAS spectra following the

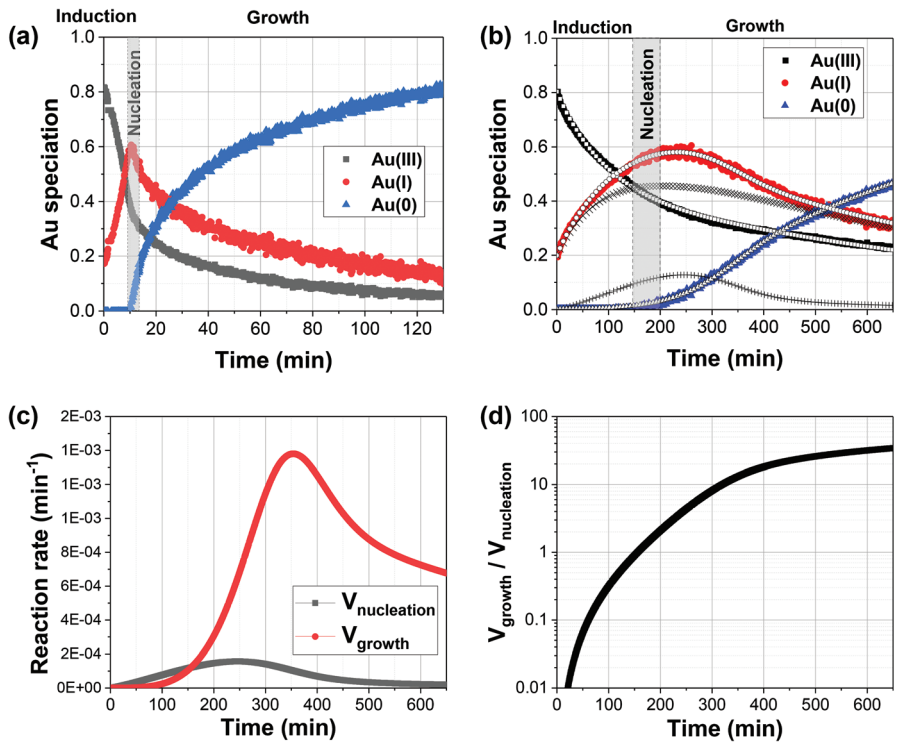

Fig. 6 Relative Au(III), Au(I) and Au(0) concentrations deduced from LCA of the *in situ* time-resolved XAS spectra at the Au L_{III}-edge during the Au nanoparticle synthesis with (a) [OY] = 100 mM and (b) [OY] = 400 mM (right). On figure (b) the open dots correspond to the best fit of the kinetic model to the XAS data, the symbols (+) and (×) correspond to the reactive and less reactive intermediate Au(I) species, respectively (see text). (c) Nucleation and growth rates as a function of time, given by the kinetic modeling of the Au nanowire synthesis with [OY] = 400 mM, according to reaction Scheme 2; (d) ratio between the growth and nucleation rates of the Au nanowire synthesis with [OY] = 400 mM.

same method as in the previous section. The corresponding XAS spectra and examples of LCA are reported in the ESI (Fig. S10†). Increasing [OY] prolongs the induction stage, Au(0) appearing after 10 min and around 180 min for [OY] = 100 mM and 400 mM, respectively. In both cases, the onset of Au(0) started when the Au(I) concentration reached the relative value of about 0.55 and [Au(I)] reached a maximum value of 0.6. Since the final particles have very different volumes, it is noteworthy that the nucleation rate is independent of [Au(I)]. An auto-catalytic model was built to describe the kinetics of the reaction with [OY] = 400 mM. For such OY concentration, the gold precursor characterization (section 3.2) showed that the initial solution contained mainly Au complexes coordinated by oleylamine. These complexes were considered as poorly reactive for the reduction by TIPS and in equilibrium with poorly reactive Au(I) species. These Au(I) species are themselves in equilibrium with reactive Au(I) species involved in the nucleation and auto-catalytic steps as in the previous model (Scheme 2). The kinetic model is described in a more detailed way in the ESI (Table S4† and corresponding text). As can be seen in Fig. 6b, this model fits very well to the variations of [Au(III)], [Au(I)] and [Au(0)] over the entire reaction. The nucleation and growth rates given by this model are plotted as a function of time in Fig. 6c. Interestingly, the modelling describes well that the nucleation stage involves only a very small amount of gold, at the opposite of the nucleation stage of the nanospheres prepared with [OY] = 50 mM. The grey shaded area in Fig. 6b corresponds to the nucleation stage. It begins at the onset of Au(0) and finishes when V_{AC} is much higher than V_N. According to the rate constants given by the fit, the growth rate becomes higher than twice the nucleation rate at 200 min and increases very quickly afterwards (Fig. 6d). The end of the nucleation stage has been taken arbitrarily at t = 200 min.

The time-resolved SAXS patterns recorded during the synthesis with [OY] = 100 mM are given in Fig. 7a for the period 4 s–20 min that covers the induction, nucleation and beginning of the growth stages, and in Fig. S12† for the complete reaction. The scattering intensity profile due to the 3.9 nm PNCs remains almost constant during the first 5 minutes (Fig. 7a). Between 5 and 14 min, there is a progressive change in the scattering intensity, with the shift of the "knee-position" to high-q. This phenomenon occurs in the time range corresponding to the onset of Au(0) in the gold speciation plot. Thus, a shrinkage of the particle size is observed at the metal particle nucleation, similarly to what has been already observed with [OY] = 50 mM, but much slowed down. After *ca.* 14 minutes, the scattering intensity increases and the knee-position shifts toward low-q, showing an increasing number of metal nanoparticles with an increasing size. The size of the PNCs and of the metal particles inferred from the fits of the SAXS patterns are given in Table S6.† A change in the scattering intensity of the Porod regime at very low-q is also noticeable between the beginning of the reaction and 30 min (Fig. S12†). The slope at low-q, revealing some secondary structures of the pre-nucleation clusters, is present during the whole induction stage. It vanishes progressively from 15 min, *i.e.* at the beginning of the growth stage, and has disappeared

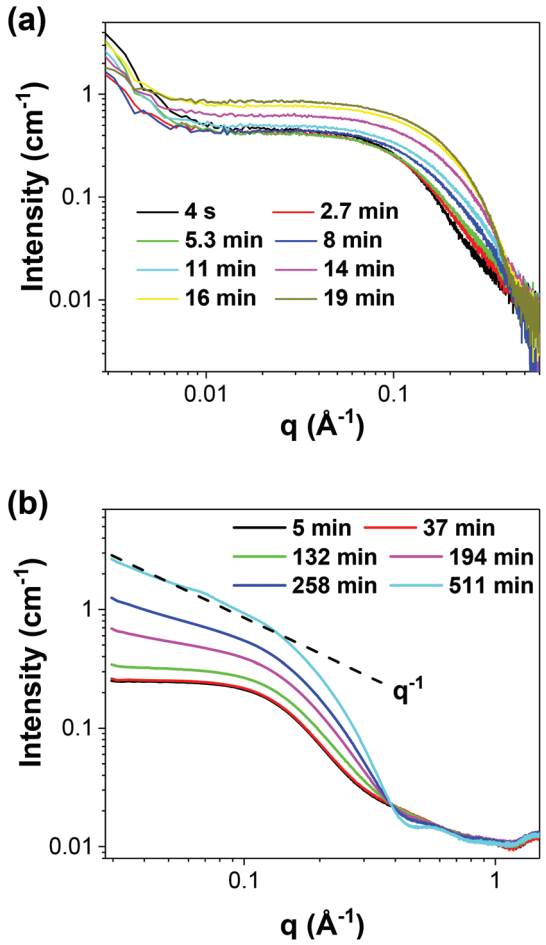

Fig. 7 *In situ* SAXS patterns recorded during the synthesis of Au nanoparticles in OY/hexane solution: (a) [OY] = 100 mM, during the first 20 minutes and (b) [OY] = 400 mM.

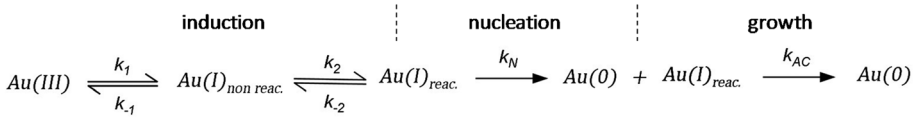

Scheme 2 Modelling of the reaction mechanism of the Au nanowires formation with [OY] = 400 mM. The Au(0) NP nucleation/growth process is modelled by an auto-catalytic process with the reaction rate constants k_N and k_{AC}. The very large excess of oleylamine in the medium favors the formation of a "non-reactive" Au(III) complex. This complex is progressively reduced into a "non-reactive" Au(I) complex in equilibrium with a reactive Au (I) complex which is finally involved in the Au(0) formation. Both "non reactive" complexes serve as a reservoir for the "reactive complexes".

after 30 min (Fig. S12†). This observation highlights that the nucleation stage occurs from PNCs involved in larger hierarchical structures. The reduction of the PNCs into metal nanoparticles destabilizes the secondary structures.

After *ca.* 40 minutes, a shift to the low-q region of the "knee-position" is observed along with an increasing scattering intensity (Fig. S12†). This last phenomenon was not observed with [OY] = 50 mM and can be interpreted as a secondary growth stage with an increasing number of bigger particles in agreement with the TEM images of the final particles showing a bimodal distribution with particles of diameter 6 nm.

Fig. 7b depicts the SAXS patterns for the synthesis with [OY] = 400 mM. The scattering intensity remains almost constant for the first 150 min. A progressive increase of the scattering intensity at low-q is then observed, in agreement with the growth of nanowires. After around 450 min, the scattering intensity at low q follows a q^{-1} power law showing that the dominant scattering objects in the medium are the nanowires.[43,46]

High-energy X-ray diffraction combined with PDF analysis is a good probe for very small particles and/or poorly crystalline compounds.[62] PDFs calculated from the *in situ* HE-XRD pattern recorded during the syntheses of the nanoparticles prepared with [OY] = 100 mM and nanowires prepared with [OY] = 400 mM are shown in Fig. 8. For both kinetics, the PDFs exhibit at the beginning of the reaction a distance at 3.38 Å in good agreement with an Au–Au aurophilic bond observed mainly in Au(I) dimers or chains, but also in some cases in Au(III) dimers.[63] For [OY] = 100 mM, after *ca.* 10 min of reaction, a well-defined PDF peak at a radial distance of 2.84 Å corresponding to the Au–Au pair distance in metal nanoparticles is also observed. This last distance is in good agreement with the distance measured by EXAFS. The PDF peak at 3.38 Å disappeared rapidly and after 1 h the PDF was similar to the one after 22 h (Fig. 8a). It shows that, after 1 h, the scattering intensity at wide angles is mainly due to the atomic correlation in the metal particles, in agreement with the SAXS and XAS results. For [OY] = 400 mM, the distance at 3.38 Å was observed during the first 150 minutes of reaction, *i.e.* covering the whole induction stage. Then, this distance progressively disappeared while at the same time progressively appeared the distance at 2.86 Å corresponding to the metal bond in the nanowires, in agreement with the LCA analysis (Fig. 8b). Unfortunately, the acquisition time of few minutes required for a good HE-XRD pattern prevented the study of the structure of the pre-nucleation clusters for the very fast reaction with [OY] = 50 mM.

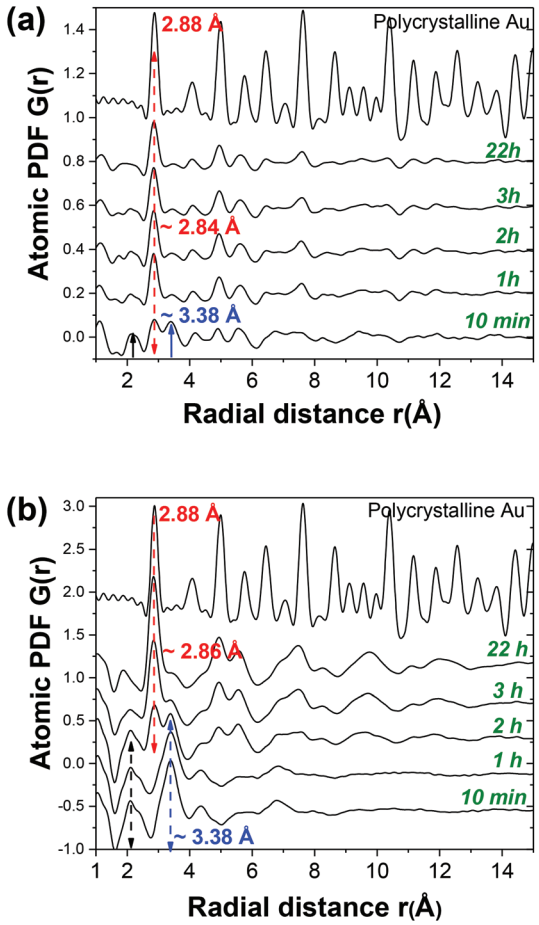

Fig. 8 *In situ* atomic PDFs as a function of time: (a) [OY] = 100 mM; (b) [OY] = 400 mM. The blue arrow highlights the Au–Au pair distances present at the beginning of the reaction as a PDF peak centered at 3.38 Å; the black arrow highlights the bonds between Au and light atoms, N or Cl, appearing as a broad PDF peak centered at about 2.15 Å; the red dotted arrow highlights the Au–Au pair distances in metal NPs appearing as a well-defined PDF peak centered at 2.84 Å and 2.86 Å.

3.5 Discussion

The reduction of gold chloride by the TIPS in hexane in the presence of different concentrations of OY leads to ultrasmall gold particles, spheres or wires, with an unusual atomic structure. The OY concentration plays a decisive role in the nucleation and growth stages. The joint XAS and SAXS studies have permitted combining chemical and morphological information during the nanoparticle synthesis and correlating the variation of morphology of the scattering objects in solution with the extent of the reaction all along the induction, nucleation and growth stages. HE-XRD has completed the study providing structural information on the precursors before nucleation and on the final gold particles.

The main result that must be highlighted here is the role of the molecular PNCs in the nucleation of the gold particles. PNCs involved in secondary structures were identified by SAXS for all OY concentrations. The PNCs shrinkage observed by SAXS is concomitant with the nucleation and the beginning of growth of the metal particles Au(0) observed by XAS. Moreover, the secondary structures attributed to van der Waals attraction between the PNCs vanish progressively during the nucleation stage. SAXS requires a contrast in the SLD between the clusters and the solvent, high enough to give a significant intensity. It shows that the core of the clusters contains Au(III) and/or Au(I) complexes. A short Au–Au distance was detected by HE-XRD during the pre-nucleation/induction stage showing an associ-

ation of Au complexes, attributed to the aurophilic bond. The surface fractal structure of the PNCs may be attributed to the presence of oleylamine in the outer shell. For the highest OY concentration, the internal structure seems quite different which could be due to the large number of OY coordinating the Au atoms, thus limiting their association. The size of the PNCs was determined by SAXS but the question then arises on assessing the number of gold atoms constituting the PNCs depending on their size. Assuming a molecular volume of the gold complex coordinated by Cl and OY of about 0.6–0.65 nm^3 (Table S1†) and assuming PNCs with a spherical shape, the ratio between the volume of the PNCs and the molecular volume of the gold complex gives from 50 to 70 units in the PNCs with a diameter of 3.9–4.4 nm, like those observed with [OY] = 50 mM, and only 15 units for the PNCs with a diameter of 2.7 nm, like those observed with [OY] = 400 mM. Gathering SAXS and XAS results, a possible description of the Au NP formation with [OY] = 50 mM is: (i) a sudden reduction of the PNCs to Au(0) nuclei containing 50 to 65 atoms, *i.e.* to a size of about 1–1.2 nm; (ii) a very fast growth with remaining highly reactive Au(I) species to give 1.9 nm NPs; (iii) and after 30 s a slower growth involving the 50% less-reactive species remaining to give finally the 2.4 nm final Au NPs. The numbers of Au atoms inside the PNCs do not take into account possible inhomogeneity of density inside the clusters, such as a core shell structure with OY chains organized as an outer shell. Hence, the molecular volume in the cluster cores could be lower and the number of Au atoms higher, but this does not change the overall description. The same scheme applies to the nucleation and first growth stage of the nanospheres prepared with [OY] = 100 mM. However, in this case, the OY excess increases the non-reactive species amount, the nucleation step involves less Au and an additional growth stage is observed leading to a bimodal size distribution. It is noteworthy, however, that the primary particles have the same size as in the case with [OY] = 50 mM, despite a much slower nucleation rate. This cannot be explained in the framework of the classical nucleation theory, as was mentioned in other systems.[27] For the nanowire synthesis, Pschunder *et al.* proposed a nucleation involving pre-nucleation clusters and reported on a size contraction at the nanowire nucleation.[46] Here, we show that the size of the clusters depends on the OY concentration and we can make the hypothesis that the PNC size and the degree of coordination with OY of the Au centers involved in the nuclei determine the nucleation rate. The biggest PNCs appear very reactive, because they contain enough Au atoms to lead to stable nuclei, whereas the smallest ones are not reactive and, as suggested by Pschunder *et al.*,[46] require an association into bigger anisotropic structures to lead to the nucleation. In both schemes, the Au(0) nuclei are not generated according to the classical nucleation theory, *i.e.* by the progressive association of Au(0) free monomers into small Au(0) clusters and then stable Au(0) nuclei, as it was described by Abécassis *et al.*[13] or by Chen *et al.*[15] for the chemical reduction of gold chloride using borohydride or borane as reductants. In the present case, the shrinkage of the pre-nucleation clusters into small Au(0) metal particles shows that the nucleation is an internal reduction of the pre-nucleation clusters.

The second particularity of this system is related to the reduction by TIPS of Au complexes coordinated or partially coordinated by OY. The LCA of the time resolved XANES spectra showed the co-existence of the three oxidation states during the growth stage whatever OY concentration, but the reaction rate constants of the different reduction steps, deduced from the kinetic modeling, are at least two orders of magnitude smaller for [OY] = 400 mM than for [OY] = 50 mM. This highlights the role of OY that not only forms an ammonium to dissolve $[AuCl_4]^-$ but also changes the reactivity of the precursors by binding to the Au ions. Kinetic modelling required the introduction of non-reactive Au(III) and Au(I) species to correctly describe experimental gold speciation. It is known from the literature that gold(I) complexes with amine and chloride ligands can adopt two kinds of coordination chemistry forming charged or neutral complexes, $[Au(RNH_2)_2]Cl$ or $(RNH_2)AuCl$, respectively.[64] Both kinds of compounds form polymeric chains like $[Au(NH_3)_2]X$[65] or (OY)AuCl.[44] In these chains, the aurophilic bond is reinforced by hydrogen bonds between NH_2 and Cl groups. With a large excess of OY, the Au(III)N_4 and Au(I)N_2 centers were evidenced by EXAFS showing the complete substitution of the chloride by OY in the Au ion coordination spheres. With a slight excess of OY, the presence of both coordination complexes is very likely.

Eqn (1) that describes the whole reduction of Au(III) to Au NPs is supported by the absence of molecular hydrogen evolution during the syntheses and by the total conversion of oleylamine to ammonium when it is added in stoichiometric amount. The gold reduction by TIPS involves hydrides as intermediates. Gold hydrides have been proposed as intermediates in gold-catalyzed reactions such as hydrogenation[66] or hydrosilylation.[67] Previous studies showed also the possibility to isolate Au(III) and Au(I) hydrides using lithium borohydride[68] or hydrosilane *via* σ-bond metathesis.[69] Thus, the first step of Au(III) and Au(I) reduction by TIPS likely proceeds *via* a σ-bond metathesis with formation of a gold hydride and triisopropyl chlorosilane, followed by a reductive elimination of a proton with the help of oleylamine to form the ammonium. The substitution of Cl by OY in the coordination spheres of the gold complexes reduces the possibility of σ-bond metathesis which could be the reason for the lower reduction rates; the reduction then occurs only through a dynamic ligand exchange in the Au coordination sphere. This hypothesis is supported by the need to introduce in the kinetic models equilibria between reactive (complexes containing chloride in the coordination sphere) and non-reactive species (complexes with only OY in the coordination sphere).

Thus, by substituting the chloride ions in the coordination sphere of the gold precursors, OY has a double effect. It slows down the reduction rates by the TIPS and notably increases the induction times, and it limits the association of the molecular complexes into large pre-nucleation clusters limiting the number of nuclei. A third effect of OY that can also contribute to slowing down the reduction rate is the formation of a

second shell of OY around the coordination sphere of the Au complexes with large OY concentration, limiting the access of the TIPS to the Au(III) and Au(I) coordination sphere. This hypothesis is supported by the fact that, in a large excess of OY, the final nanowires are surrounded by a bilayer of oleylammonium/oleylamine, as it was reported in previous studies.[43] This bilayer was also described as responsible for the anisotropic growth through the formation of cylindrical micelles around the wires. A fourth effect that has not been considered here is the reducing power of OY assuming that Au(III) and Au (I) complexes are reduced by OY at higher temperature.[31]

4. Conclusion

The nucleation/growth mechanism evidenced for the nanosphere formation can be summarized as follows: formation of non-reduced PNCs; progressive reduction from Au(III) to Au(I) inside the clusters without significant PNC size modification; abrupt size shrinkage of the PNCs into metal nuclei containing approximately 50–60 atoms; fast growth involving reactive Au complexes followed by a slow growth involving non-reactive complexes acting as a reservoir. In the case of nanospheres, the PNCs are large enough and/or enough reactive to allow the nucleation directly from PNCs. In the presence of an excess of OY the PNCs are smaller and less reactive, limiting the nucleation and slowing down the growth. This mechanism is consistent with a previous study on the nanowire formation that described the association of prenucleation clusters into anisotropic objects before the metal NW nucleation. The classical nucleation theory does not apply for these systems since the number of nuclei depends more on the size and reactivity of the PNCs rather than on a concentration threshold of zerovalent gold atoms. The multiple roles of OY have been clarified thanks to this study. The complete substitution of chloride ions by OY in the Au coordination sphere not only limits the clustering but also hinders the action of TIPS preventing the formation of hydrides through metathesis.

The PNCs in this study have still an ill-defined formula $[Au_xCl_yOY_z]_n$. In future studies, it will be interesting to improve the structural characterization of the PNCs at the atomic/molecular scale. A better assessment of the number of Au atoms involved in the nucleation stage will be useful to complete the mechanism description because the kinetic modeling including an autocatalytic process, although very useful for demonstrating the presence of non-reactive species acting as reservoirs, does not include information on the size of the nuclei. A prospect for this work is to extend the study to other systems exhibiting reactive metal–organic PNCs and try defining new rational routes of ultrasmall nanoparticles and ultrathin nanowires with non-classical structures.

Conflicts of interest

There are no conflicts to declare.

Acknowledgements

The authors thank M. Impéror-Clerc, Laboratoire de Physique des Solide, CNRS-Université Paris Saclay, and Q. Kong, SOLEIL, for fruit full discussions about SAXS and XAS. RKR acknowledges Fédération FERMaT (Université de Toulouse) for financial support during his post-doctoral stint. The authors thank SOLEIL for providing synchrotron radiation facilities at SWING and at ODE beamlines (Proposal No.: 20171002) as well as J. Perez and Q. Kong for the assistance provided for the use of the beam lines. The authors thank PSI, Switzerland, for providing synchrotron radiation facilities at c-SAXS beamline (Proposal No.: E190700304) as well as Ana Diaz for the assistance provided for the use of the beam line. This work used resources of the Advanced Photon Source at the Argonne National Laboratory provided by the DOE Office of Science under contract no. DE-AC02-06CH11357. Thanks are due to Dr K. Beyer for the help with the HE-XRD experiments. This project has received funding from the European Union's Horizon 2020 research and innovation program under grant agreement no. 731019 (EUSMI). The work was supported in part by DOE-BES grant DE-SC0006877.

References

1 J. Park, J. Joo, S. G. Kwon, Y. Jang and T. Hyeon, *Angew. Chem., Int. Ed.*, 2007, **46**, 4630–4660.
2 D. Huo, M. J. Kim, Z. Lyu, Y. Shi, B. J. Wiley and Y. Xia, *Chem. Rev.*, 2019, **119**(15), 8972–9073.
3 M. R. Axet and K. Philippot, *Chem. Rev.*, 2020, **120**, 1085–1145.
4 P. K. Jain, X. Huang, I. H. El-Sayed and M. A. El-Sayed, *Acc. Chem. Res.*, 2008, **41**, 1578–1586.
5 A. Kamyshny and S. Magdassi, *Small*, 2014, **10**, 3515–3535.
6 K. An and G. A. Somorjai, *ChemCatChem*, 2012, **4**, 1512–1524.
7 Y. Xia, K. D. Gilroy, H.-C. Peng and X. Xia, *Angew. Chem., Int. Ed.*, 2017, **56**, 60–95.
8 W. Niu, L. Zhang and G. Xu, *Nanoscale*, 2013, **5**, 3172–3181.
9 N. T. K. Thanh, N. Maclean and S. Mahiddine, *Chem. Rev.*, 2014, **114**, 7610–7630.
10 E. V. Shevchenko, D. V. Talapin, H. Schnablegger, A. Kornowski, Ö. Festin, P. Svedlindh, M. Haase and H. Weller, *J. Am. Chem. Soc.*, 2003, **125**, 9090–9101.
11 J. Polte, T. T. Ahner, F. Delissen, S. Sokolov, F. Emmerling, A. F. Thunemann and R. Kraehnert, *J. Am. Chem. Soc.*, 2010, **132**, 1296–1301.
12 T. J. Woehl, J. E. Evans, I. Arslan, W. D. Ristenpart and N. D. Browning, *ACS Nano*, 2012, **6**, 8599–8610.
13 B. Abécassis, F. Testard, O. Spalla and P. Barboux, *Nano Lett.*, 2007, **7**, 1723–1727.
14 B. Abécassis, F. Testard, Q. Kong, F. Baudelet and O. Spalla, *Langmuir*, 2010, **26**, 13847–13854.
15 X. Chen, J. Schröder, S. Hauschild, S. Rosenfeldt, M. Dulle and S. Förster, *Langmuir*, 2015, **31**, 11678–11691.

16 M. A. Watzky and R. G. Finke, *J. Am. Chem. Soc.*, 1997, **119**, 10382–10400.
17 E. E. Finney and R. G. Finke, *J. Colloid Interface Sci.*, 2008, **317**, 351–374.
18 A. Henglein and M. Giersig, *J. Phys. Chem. B*, 2000, **104**, 6767–6772.
19 L. Colombi Ciacchi, W. Pompe and A. De Vita, *J. Am. Chem. Soc.*, 2001, **123**, 7371–7380.
20 T. Yao, Z. Sun, Y. Li, Z. Pan, H. Wei, Y. Xie, M. Nomura, Y. Niwa, W. Yan, Z. Wu, Y. Jiang, Q. Liu and S. Wei, *J. Am. Chem. Soc.*, 2010, **132**, 7696–7701.
21 D. Gebauer and H. Cölfen, *Nano Today*, 2011, **6**, 564–584.
22 J. J. De Yoreo, P. U. P. A. Gilbert, N. A. J. M. Sommerdijk, R. L. Penn, S. Whitelam, D. Joester, H. Zhang, J. D. Rimer, A. Navrotsky, J. F. Banfield, A. F. Wallace, F. M. Michel, F. C. Meldrum, H. Colfen and P. M. Dove, *Science*, 2015, **349**, aaa6760.
23 J. Russo and H. Tanaka, *MRS Bull.*, 2016, **41**, 369–374.
24 J. Lee, J. Yang, S. G. Kwon and T. Hyeon, *Nat. Rev. Mater.*, 2016, **1**, 1–16.
25 S. Karthika, T. K. Radhakrishnan and P. Kalaichelvi, *Cryst. Growth Des.*, 2016, **16**, 6663–6681.
26 R. Demichelis, P. Raiteri, J. D. Gale, D. Quigley and D. Gebauer, *Nat. Commun.*, 2011, **2**, 1–8.
27 B. Fleury, M.-A. Neouze, J.-M. Guigner, N. Menguy, O. Spalla, T. Gacoin and D. Carriere, *ACS Nano*, 2014, **8**, 2602–2608.
28 N. D. Loh, S. Sen, M. Bosman, S. F. Tan, J. Zhong, C. A. Nijhuis, P. Kŕal, P. Matsudaira and U. Mirsaidov, *Nat. Chem.*, 2017, **9**, 77–87.
29 Y. Mikhlin, M. Likhatski, A. Karacharov, V. Zaikovski and A. Krylov, *Phys. Chem. Chem. Phys.*, 2009, **11**, 5445–5454.
30 Y. Mikhlin, A. Karacharov, M. Likhatski, T. Podlipskaya, Y. Zubavichus, A. Veligzhanin and V. Zaikovski, *J. Colloid Interface Sci.*, 2011, **362**, 330–336.
31 M. V. Kirichkov, A. A. Guda, A. P. Budnyk, T. A. Lastovina, A. L. Bugaev, V. V. Shapovalov, Y. V. Rusalev, A. V. Chernyshev and A. V. Soldatov, *J. Struct. Chem.*, 2017, **58**, 1403–1410.
32 L. Polavarapu, S. Mourdikoudis, I. Pastoriza-Santos and J. Pérez-Juste, *CrystEngComm*, 2015, **17**, 3727–3762.
33 L. Wu, A. Mendoza-Garcia, Q. Li and S. Sun, *Chem. Rev.*, 2016, **116**, 10473–10512.
34 V. B. Nguyen, M. Benoit, N. Combe and H. Tang, *Phys. Chem. Chem. Phys.*, 2017, **19**, 4636–4647.
35 N. Liakakos, B. Cormary, X. Li, P. Lecante, M. Respaud, L. Maron, A. Falqui, A. Genovese, L. Vendier, S. Koïnis, B. Chaudret and K. Soulantica, *J. Am. Chem. Soc.*, 2012, **134**, 17922–17931.
36 S. Mourdikoudis and L. M. Liz-Marzán, *Chem. Mater.*, 2013, **25**, 1465–1476.
37 B. Cormary, T. Li, N. Liakakos, L. Peres, P. F. Fazzini, T. Blon, M. Respaud, A. J. Kropf, B. Chaudret, J. T. Miller, E. A. Mader and K. Soulantica, *J. Am. Chem. Soc.*, 2016, **138**, 8422–8431.
38 H. Feng, Y. Yang, Y. You, G. Li, J. Guo, T. Yu, Z. Shen, T. Wu and B. Xing, *Chem. Commun.*, 2009, 1984.
39 A. Sánchez-Iglesias, B. Rivas-Murias, M. Grzelczak, J. Pérez-Juste, L. M. Liz-Marzán, F. Rivadulla and M. A. Correa-Duarte, *Nano Lett.*, 2012, **12**, 6066–6070.
40 J. H. M. Maurer, L. González-García, B. Reiser, I. Kanelidis and T. Kraus, *ACS Appl. Mater. Interfaces*, 2015, **7**, 7838–7842.
41 S. Gong, W. Schwalb, Y. Wang, Y. Chen, Y. Tang, J. Si, B. Sirinzadeh and W. Cheng, *Nat. Commun.*, 2014, **5**, 1–8.
42 J. A. Vargas, V. Petkov, E. S. A. Nouh, R. K. Ramamoorthy, L.-M. Lacroix, R. Poteau, G. Viau, P. Lecante and R. Arenal, *ACS Nano*, 2018, **12**, 9521–9531.
43 A. Loubat, M. Impéror-Clerc, B. Pansu, F. Meneau, B. Raquet, G. Viau and L.-M. Lacroix, *Langmuir*, 2014, **30**, 4005–4012.
44 A. Loubat, L.-M. Lacroix, A. Robert, M. Impéror-Clerc, R. Poteau, L. Maron, R. Arenal, B. Pansu and G. Viau, *J. Phys. Chem. C*, 2015, **119**, 4422–4430.
45 M. Saitoh, Y. Kashiwagi and M. Chigane, *Soft Matter*, 2017, **13**, 3927–3935.
46 F. Pschunder, J. Puig, L. J. Giovanetti, C. Huck-Iriart, F. G. Requejo, D. Buceta, C. E. Hoppe and J. M. Ramallo-López, *J. Phys. Chem. C*, 2018, **122**, 29051–29061.
47 L. Falk and J. M. Commenge, *Chem. Eng. Sci.*, 2010, **65**, 405–411.
48 G. Beaucage, *J. Appl. Crystallogr.*, 1996, **29**, 134–146.
49 B. Ravel and M. Newville, *J. Synchrotron Radiat.*, 2005, **12**, 537–541.
50 M. Newville, *J. Phys.: Conf. Ser.*, 2013, **430**, 012007.
51 S. J. A. Figueroa and C. Prestipino, *J. Phys.: Conf. Ser.*, 2016, **712**, 012012.
52 J. Strähle, J. Gelinek and M. Kölmel, *Z. Anorg. Allg. Chem.*, 1979, **466**, 241–260.
53 A. Ankudinov, A. Nesvizhskii and J. Rehr, *Phys. Rev. B: Condens. Matter Mater. Phys.*, 2003, **67**, 115120.
54 W. Szczerba, H. Riesemeier and A. F. Thünemann, *Anal. Bioanal. Chem.*, 2010, **398**, 1967–1972.
55 *NIST database*.
56 El S. Nouh, E. Baquero, L.-M. Lacroix, F. Delpech, R. Poteau and G. Viau, *Langmuir*, 2017, **33**, 5456–5463.
57 P. G. Jones, *Gold Bull.*, 1981, **14**, 102–118.
58 P. G. Jones, R. Hohbein and E. Schwarzmann, *Acta Crystallogr., Sect. C: Cryst. Struct. Commun.*, 1988, **44**, 1164–1166.
59 C. J. Serpell, J. Cookson, D. Ozkaya and P. D. Beer, *Nat. Chem.*, 2011, **3**, 478–483.
60 Z. Huo, C. Tsung, W. Huang, X. Zhang and P. Yang, *Nano Lett.*, 2008, **8**, 2041–2044.
61 Z. Li, J. Tao, X. Lu, Y. Zhu and Y. Xia, *Nano Lett.*, 2008, **8**, 3052–3055.
62 V. Petkov, *Mater. Today*, 2008, **11**, 28–38.
63 H. Schmidbaur and A. Schier, *Chem. Soc. Rev.*, 2012, **41**, 370–412.

64 P. G. Jones and B. Ahrens, *New J. Chem.*, 1998, 1041–1042.
65 S.-L. Zheng, C. L. Nygren, M. Messerschmidt and P. Coppens, *Chem. Commun.*, 2006, 3711–3713.
66 A. Comas-Vives, C. González-Arellano, A. Corma, M. Iglesias, F. Sánchez and G. Ujaque, *J. Am. Chem. Soc.*, 2006, **128**, 4756–4765.
67 A. Corma, C. González-Arellano, M. Iglesias and F. Sánchez, *Angew. Chem., Int. Ed.*, 2007, **46**, 7820–7822.
68 D.-A. Roşca, D. A. Smith, D. L. Hughes and M. Bochmann, *Angew. Chem., Int. Ed.*, 2012, **51**, 10643–10646.
69 E. Y. Tsui, P. Müller and J. P. Sadighi, *Angew. Chem., Int. Ed.*, 2008, **47**, 8937–8940.